RESEARCH ARTICLE

ADVANCED FUNCTIONAL MATERIALS
www.afm-journal.de

Au@h-BN Core–Shell Nanostructure as Advanced Shell-Isolated Nanoparticles for In Situ Electrochemical Raman Spectroscopy in Alkaline Environments

*Jee Hyeon Kim, Jihyun Ra, Younghee Park, Junyeon Yoon, Eunji Lee, and Hyunseob Lim**

Recent advancements in in situ electrochemical Raman spectroscopy using shell-isolated nanoparticles have facilitated direct analysis of electrochemical mechanisms. However, shell materials such as SiO_2 and Al_2O_3 commonly adopted for shell-isolated nanoparticle-enhanced Raman spectroscopy are unstable and unreliable in alkaline environments, posing significant obstacles for relevant research in the alkaline environment. While alternative shell materials have been explored, finding suitable replacements for traditional SiO_2 shells is still challenging. To address this issue, this study proposes hexagonal boron nitride (h-BN), with atomically ultrathin and insulating properties, as an alternative shell material. Specifically, pinhole-free Au nanoparticles coated by an h-BN shell (Au@h-BN) with a uniform thickness of 1 nm are synthesized through a controlled two-step process. The resulting Au@h-BN exhibits more pronounced Raman scattering and long-term stability under alkaline conditions compared to Au@SiO_2. Theoretical simulations support a stronger electromagnetic field distribution around Au@h-BN compared to that around Au@SiO_2. In situ Raman studies conducted during electrochemical reactions of Ni and Cu electrodes demonstrate the superior Raman enhancement effect and durability of Au@h-BN compared to Au@SiO_2. These results suggest that Au@h-BN holds significant potential for advancing long-term in situ Raman studies in alkaline systems, supporting the development of efficient catalysts for sustainable energy applications.

1. Introduction

Electrochemical processes stand at the core of diverse energy applications, including batteries,[1] fuel cells,[2] hydrogen generators,[3] ammonia synthesis,[4] and CO_2 reduction systems,[5] all of which are central to the development of sustainable energy solutions.[6] In recent years, in situ Raman spectroscopy has emerged as a powerful technique for acquiring in-depth insights into molecular vibrations and interactions under realistic conditions, rendering it highly effective for the exploration of electrochemical mechanisms. Nevertheless, the inherently weak Raman scattering cross-section obscures the precise detection of chemical species on the electrode surface. To overcome this challenge, localized surface plasmon resonance (LSPR) has been employed to enhance the Raman signal. Originally proposed in 1974 in the context of electrochemical reactions on roughened silver electrodes,[7] LSPR paved the way for surface-enhanced Raman spectroscopy (SERS) using plasmonic metal nanoparticles (NPs). This approach further evolved into shell-isolated nanoparticle-enhanced Raman spectroscopy (SHINERS), wherein a dielectric shell isolated the metal NP from direct contact with the target analyte. By splitting unwanted electrochemical reactions, this configuration reduces background noise and bolsters both stability and reproducibility. Since its inception in 2010,[8] SHINERS has gained widespread attraction for investigating complex electrochemical phenomena, offering profound insights into their underlying mechanisms.

Over the past decade, the field of in situ electrochemical study combined with SHINERS (EC-SHINERS) has seen remarkable advancements not only in instrumentation and in situ cell design but also shell engineering. Nonetheless, the majority of SHINs are still predominantly fabricated using SiO_2 and Al_2O_3 shells, with certain inherent limitations. Therefore, other metal oxide materials, including MnO_2,[9] TiO_2,[10] SnO_2,[11] and ZrO_2,[12] have also been proposed as alternatives. Despite these suggestions, the isotropic crystal structures of metal oxides lead to thermodynamic instability in atomically thin structures, making it difficult to achieve ultrathin, pinhole-free shells, especially with

J. H. Kim, J. Ra, Y. Park, E. Lee, H. Lim
Department of Chemistry
Gwangju Institute of Science and Technology (GIST)
Gwangju 61005, Republic of Korea
E-mail: hslim17@gist.ac.kr

J. H. Kim, J. Ra, H. Lim
Center for Quantum Conversion Research (QCR)
Institute of Basic Science (IBS)
Gwangju 61005, Republic of Korea

J. Ra, J. Yoon, E. Lee
School of Materials Science and Engineering
Gwangju Institute of Science and Technology (GIST)
Gwangju 61005, Republic of Korea

The ORCID identification number(s) for the author(s) of this article can be found under https://doi.org/10.1002/adfm.202504706

DOI: 10.1002/adfm.202504706

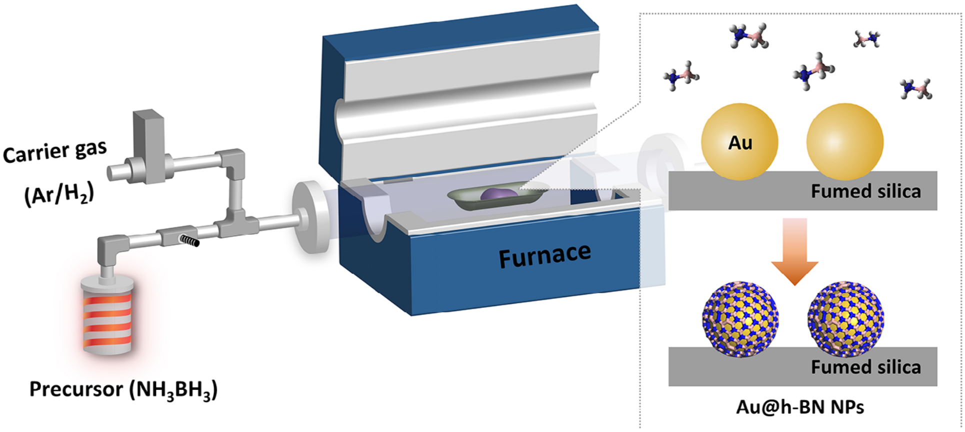

Scheme 1. Schematic depicting the synthesis process for Au@h-BN NPs in a CVD system.

thicknesses below 2nm, although it is of great significance to improve the detection sensitivity of surface-adsorbed molecules.[13] Additionally, the limited stability of these ceramic material-based shells in strongly alkaline environments limits their applicability under extreme electrochemical conditions. To address these issues, alternative shell materials including 2D materials were suggested for increasing stability in alkaline solution.[14] The absence of dangling bonds on 2D material surfaces offers several advantages such as atomically thin thickness, chemical stability, and chemical inertness. Among the various 2D materials, hexagonal boron nitride (h-BN) has emerged as an ideal candidate as shell material for SHINs in in situ electrochemical study due to its insulating electronic characteristics and exceptional chemical stability. However, while graphite shells have been explored,[15] h-BN shells have not yet been demonstrated for SHINs.

In this work, we report a synthetic method to produce h-BN-encapsulated AuNPs (Au@h-BN), forming a core–shell structure that delivers notable advantages. Remarkably, the synthesized Au@h-BN NPs not only show structural stability without any pinholes but also exhibit improved Raman scattering enhancement effects compared to the conventional Au@SiO$_2$ SHINs. We also demonstrate the robust, long-term stability of Au@h-BN in in situ Raman studies under alkaline conditions, effectively overcoming the limitations of conventional SHINs for the first time. Although some studies have shown that alternative metal oxides shells such as MnO$_2$, SnO$_2$, and ZrO$_2$ can be more stable than SiO$_2$ shells under alkaline conditions in previous literature.[9–12] While these demonstrate the feasibility of these oxide shells in alkaline media, there remain key limitations. Their surface charge states vary significantly with pH, affecting the orientation and coverage of adsorbed analytes and thus complicating spectral analysis. MnO$_2$ can also work as a catalyst for oxygen reduction and evolution (ORR and OER),[16] while SnO$_2$ is active as a catalyst in CO$_2$ and N$_2$ reduction,[17] both potentially obscuring baseline electrode reactions. Their typical Raman enhancement factors reported in the literature have generally been lower than those of Au@SiO$_2$. In contrast, the h-BN shell offers extraordinary chemical inertness and structural robustness compared to these metal oxide shells even under strongly alkaline conditions. Owing to the lack of dangling bonds, h-BN remains nonreactive and does not undergo redox reactions that could interfere with sensitive target electrochemical measurements. Consequently, we believe that Au@h-BN would be more suitable for long-duration, high-pH EC-SHINERS measurements, enabling stable and artifact-free in situ monitoring of electrode reactions in alkaline media. Overall, our approach involving the use of Au@h-BN NPs is anticipated to enhance the utility of molecular analyses across various scientific fields and promote the development of innovative methodologies in electrochemical research.

2. Results and Discussion

2.1. Synthesis and Characterization of Au@h-BN NPs

Au@h-BN NPs were synthesized through a controlled two-step process. The first step involved the wet-chemical synthesis of AuNPs solution with a size of 80 nm, while the second step involved chemical vapor deposition (CVD) to encapsulate the Individual AuNPs within an ultrathin h-BN shell. The wet-chemical synthesis of AuNPs relied on a modified seed-mediated method.[18] During this process, the diameter of the AuNPs was regulated to 80 nm by adjusting the concentration of HAuCl$_4$. The prepared AuNPs solution was then mixed with fumed silica powder as the supporting ceramic material. Subsequently, a few layers of h-BN were grown on the individual AuNPs using borane-ammonia complex (NH$_3$BH$_3$) as the precursor at a growth temperature of 1100 °C under an Ar/H$_2$ atmosphere in a CVD furnace (**Scheme 1**). Following the synthesis of Au@h-BN NPs, the supporting silica was removed through dissolution in hydrogen fluoride (HF) solution and centrifugation. The samples were then cleaned through deionized water (DW) and centrifugal separations (see the Experimental Section in Supporting Information for a detailed preparation process). Finally, the pellet collected after the final centrifugation was dissolved in a small amount of DW. This solution containing the synthesized Au@h-BN NPs was then characterized by various spectroscopic and microscopic techniques. In the UV–vis spectra of the original AuNPs, exhibiting an average size of 79.5 ± 0.8 nm (Figure S1a,b, Supporting Information), a strong absorbance peak appears at 548 nm (**Figure** 1a, black). Meanwhile, in the UV–vis spectra of the Au@h-BN, this peak undergoes a redshift to 554 nm and demonstrates slight width broadening (Figure 1a, purple). These

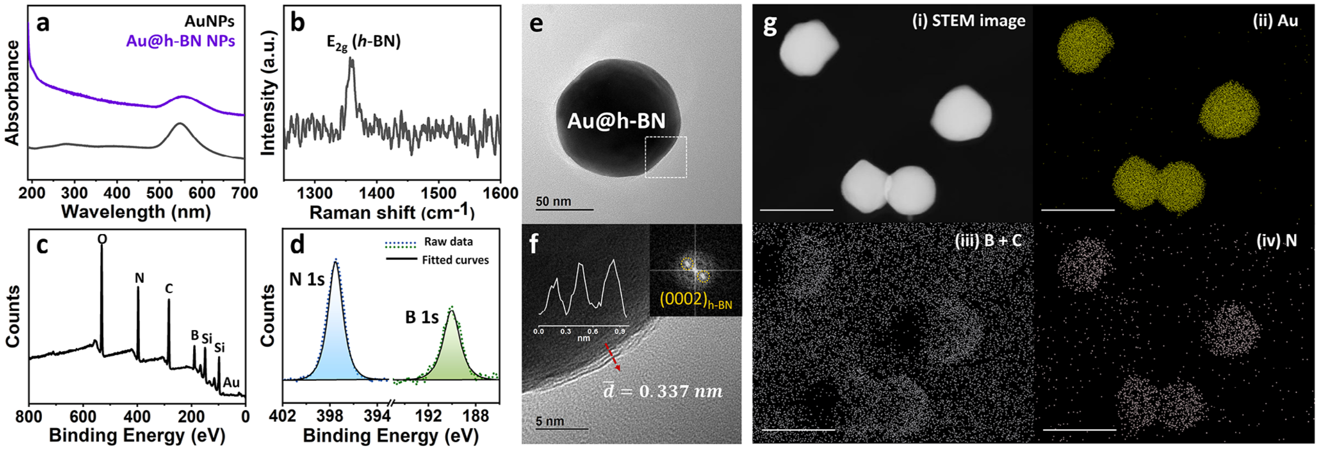

Figure 1. Characterization of Au@h-BN NPs. a) UV–vis spectra of bare AuNPs (black) and Au@h-BN NPs (purple). b) Raman spectrum of Au@h-BN. c) Survey XPS spectrum of Au@h-BN NPs on SiO_2/Si substrate. d) High-resolution XPS spectra of N 1s and B 1s orbitals. Dotted lines denote the raw data, while straight lines denote the simulated peaks. e) TEM image of 100 nm Au@h-BN NP. f) HR-TEM image of the region highlighted by a white dotted box in Figure 1e. (Inset) FFT image and line profile of the h-BN shell along the red dotted-arrow in Figure 1f. g) Scanning TEM image (i) and EDS mapping images of Au (ii), B (iii), and N (iv). Scale bar: 100 nm.

changes suggest moderate aggregation of the AuNPs at a high temperature before the growth of the h-BN shell in the CVD furnace. Notably, an additional weak peak appears ≈202 nm, indicative of h-BN absorption.[19] Our next analysis focused on assessing the size distribution of Au@h-BN NPs using scanning electron microscopy (SEM). The average size of the Au@h-BN NPs was determined to be 99.1 ± 0.7 nm, indicating an increase in the size of AuNPs during h-BN growth (Figure S1c,d, Supporting Information). To affirm the presence of the h-BN shell, various additional characterizations were performed. The Raman spectrum of Au@h-BN corroborates this, clearly depicting a prominent peak at 1360 cm^{-1}, corresponding to the E_{2g} phonon mode of h-BN (Figure 1b).[19] In the survey X-ray photoelectron spectroscopy (XPS) spectra of Au@h-BN (Figure 1c) display various peaks related to Au@h-BN and SiO_2/Si substrate. Particularly, high-resolution (HR) XPS spectra of N 1s and B 1s photoelectrons show prominent peaks at 397.5 and 190.0 eV (Figure 1d), respectively, consistent with those observed in h-BN.[19,20] Transmission electron microscopy (TEM) analyses provided more direct evidence confirming the presence of the h-BN shell on the AuNPs (Figure 1e,f). HR-TEM image of Au@h-BN NPs as shown in Figure 1f reveals the presence of layered structures on the surface of AuNP, with an interlayer spacing of 0.337 nm. This value is consistent with the *d*-spacing of the (0002) planes for h-BN.[21] Hence, two spots marked by yellow circles in the inset of Figure 1f, which depicts a fast Fourier transform (FFT) image, correspond to the (0002) planes of h-BN. Notably, most AuNPs are enveloped by three layers of h-BN, while a few are enclosed by four layers of h-BN (Figures S2 and S3, Supporting Information). The presence of h-BN shells on the AuNPs was further confirmed through a spatially resolved elemental analysis using energy-dispersive X-ray spectroscopy (EDS). The EDS mapping images displayed in Figure 1g indicate the presence of B and N elements onto AuNPs. However, resolution limitations prevent clear distinctions between the characteristic X-rays originating from the B 1s and C 1s core levels (Figure S4, Supporting Information).[22] Hence, the intensity observed in regions surrounding the AuNPs in Figure 1g(iii) is primarily attributed to the C 1s signal emitted by the thin carbon film of the TEM grid, rather than the B 1s signals. These analytical results conclusively demonstrate that the specified synthesis conditions yield AuNPs that are uniformly encased in tri-layered h-BN shells, offering potential enhancements in stability and functionality across various applications.

Notably, the growth temperature for the h-BN shells in our study was set at 1100 °C, which exceeds the melting point of 100 nm-sized AuNPs (1064 °C).[23] Consequently, the growth mechanism of the h-BN shell likely follows the vapor-liquid-solid (VLS) process (Figure S5, Supporting Information), similar to the growth mechanism of the h-BN film on a liquid Au substrate.[24] During the CVD process, the pristine AuNPs may undergo melting at 1100 °C, forming liquid-phase Au nanodroplets. However, the supporting silica powder can help prevent the coalescence of Au nanodroplets. As confirmed by previous analyses through SEM, the average size of the AuNPs increased from ≈80 to 100 nm after the CVD process, likely owing to Ostwald ripening.[25] Larger particles can form under certain conditions, but we remove these outliers via centrifugation. Consequently, while the overall size distribution broadens slightly compared to the initial solution, it remains fairly narrow, as confirmed in the histogram shown in Figure S1 (Supporting Information). Previous studies indicate that only a monolayer h-BN can be grown using a liquid Au substrate owing to the poor solubilities of B and N in liquid Au.[24] In contrast, the Au@h-BN NPs synthesized in this study are enclosed within a uniform tri-layered h-BN shell, deviating from the typical growth behavior observed when using bulk liquid Au. Numerous studies have demonstrated that the physical properties of metal NPs depend on their sizes.[26] Due to their small size and high curvature, AuNPs exhibit significantly higher surface energy compared to bulk Au. Additionally, catalytic activity levels on the surface of Au nanodroplets, as well as the solubility of B and N in these nanodroplets, likely exceed those in bulk liquid Au. Although there are no direct studies on the solubility of B and N in AuNPs, similar findings have been

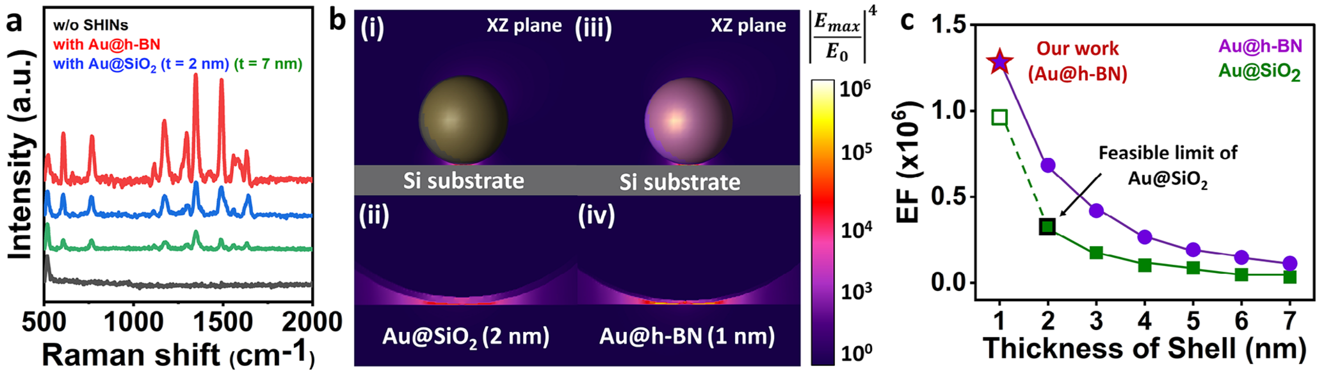

Figure 2. Raman scattering enhancement effect of Au@h-BN compared with transitional Au@SiO$_2$ NPs. a) Raman spectra of 10^{-5} $\underline{\text{M}}$ R6G without SHINs (black) and with Au@h-BN NPs ($t_{\text{h-BN}} \approx 1$ nm, red), Au@SiO$_2$ NPs ($t_{SiO2} = 2$ nm, blue), and Au@SiO$_2$ NPs ($t_{SiO2} = 7$ nm, green) on Si substrate. b) Front-view FDTD simulation images of 100 nm AuNP encapsulated by a thin shell of varying thicknesses: 2 nm-thick SiO$_2$ shell in Au@SiO$_2$ (i, ii) and 1 nm-thick h-BN shell in Au@h-BN (iii, iv) on Si substrate. c) EM field enhancement profiles of h-BN (purple) and SiO$_2$ shells (green) of varying thicknesses, ranging from 1 to 7 nm. Filled symbols denote a pinhole-free condition, while empty symbol denotes the presence condition of a pinhole.

reported for carbon solubility.[27] For instance, research has shown that carbon solubility increases dramatically at the nanoscale, causing unexpected volume changes in AuNPs. This supports the conclusion that high surface energy and enhanced atomic diffusion in NPs can facilitate multilayer growth. TEM images in Figure S2 (Supporting Information) show the Au@h-BN with a core size of ≈60 nm (Figure S2a–c, Supporting Information) and ≈110 nm (Figure S2d–f, Supporting Information), respectively. While 6–10 layers (2–3 nm) of h-BN shells were confirmed on ≈60 nm Au NP, 1–2 layers (<1 nm) of h-BN shells were only confirmed on the ≈110 nm AuNPs. In our work, the resulting Au@h-BN shells typically consisted of 3–4 layers (≈1 nm) of h-BN (Figures S2g and S3, Supporting Information). This finding supports also the idea that shell thickness can be influenced by the curvature of the AuNPs. Therefore, we believe that these factors contribute to the successful multilayer growth of h-BN on Au nanodroplets. In terms of reproducibility for SHINs preparation, the uniform thickness of the h-BN shell achieved by our approach is a significant advantage over conventional SiO$_2$-based SHINs, which require precise control over shell thickness.

2.2. Properties of Au@h-BN as SHINs

To obtain SHINs demonstrating optimal performance in in situ electrochemical Raman analysis, they must satisfy several critical criteria. For instance, the SHINs must exhibit robust Raman scattering enhancement, possess a pinhole-free structure, and demonstrate long-term stability in both acidic and alkaline environments. To investigate the Raman signal enhancement effect of the synthesized Au@h-BN NPs, we conducted a Raman analysis of rhodamine 6G (R6G) using Au@h-BN NPs and compared the obtained results with those of Au@SiO$_2$ NPs. AuNPs were synthesized with SiO$_2$ shell thicknesses of 2 and 7 nm, respectively. As illustrated in **Figure** 2a, the Au@SiO$_2$ NPs with a thinner shell (2 nm) exhibited a stronger signal enhancement effect in Raman compared to those with a thicker shell (7 nm).[28] Intriguingly, Au@h-BN NPs (≈1 nm) exhibited even greater peak intensities compared to Au@SiO$_2$ with a 2 nm shell, despite their similar shell thicknesses. This suggests that the h-BN shell is the more efficient insulating shell material for SHINs compared to Au@SiO$_2$. Notably, shell materials with high refractive index are known to boost the Raman scattering enhancement effects of core metal NPs in SHINERS fields. In this context, the high-frequency dielectric constant of amorphous SiO$_2$ (ε_∞) ranges from 2.0 to 2.2,[29] while its static dielectric constant (ε_0) is ≈3.9.[30] In contrast, the dielectric constant of h-BN varies depending on the crystallographic direction due to its anisotropy properties. Specifically, the dielectric constant of h-BN in the out-of-plane direction ($\varepsilon_{(\perp,\infty)}$) is 3.03, while in the in-plane direction ($\varepsilon_{(\parallel,\infty)}$), it is 4.98.[31] Using these values, we conducted finite-difference time-domain (FDTD) simulations to comprehend the more pronounced Raman signal enhancement effects of Au@h-BN over those of Au@SiO$_2$, as evidenced by experiment data. It is noteworthy that atomically thin h-BN features a slightly lower dielectric constant than bulk h-BN.[31] However, given that the dielectric constant of atomically thin SiO$_2$ is unknown, we used the bulk dielectric constant of h-BN and SiO$_2$ in the FDTD simulations for consistency. In FDTD calculations, the shell thickness in Au@h-BN and Au@SiO$_2$ was determined based on the minimum effective thicknesses of the shell materials for SHINERS as practical applications (h-BN: 1 nm and SiO$_2$: 2 nm),[32] corresponding to the pinhole-free thickness of the Au@h-BN and Au@SiO$_2$ experimentally verified in **Figure** 3a,e. Partially, Figure 2b shows the electromagnetic (EM) field distribution of Au@SiO$_2$ (2 nm) and Au@h-BN (1 nm), respectively, indicating that the EM field is maximum at the interface between the single SHIN and Si substrate. The EM field around Au@h-BN is stronger than that around Au@SiO$_2$. Here, the enhancement factor (EF) of the SHINs was calculated using the following simple Equation (1):

$$EF = \left|\frac{E_{max}}{E_0}\right|^4 \tag{1}$$

Using this formula, the theoretical EF of Au@h-BN was estimated to be 1.28×10^6, while that of Au@SiO$_2$ was estimated to be 3.30×10^5. Here, E_{max} values were calculated based on the maximum EM field values generated between the SHIN monomer and substrate from the FDTD results. These experimental and

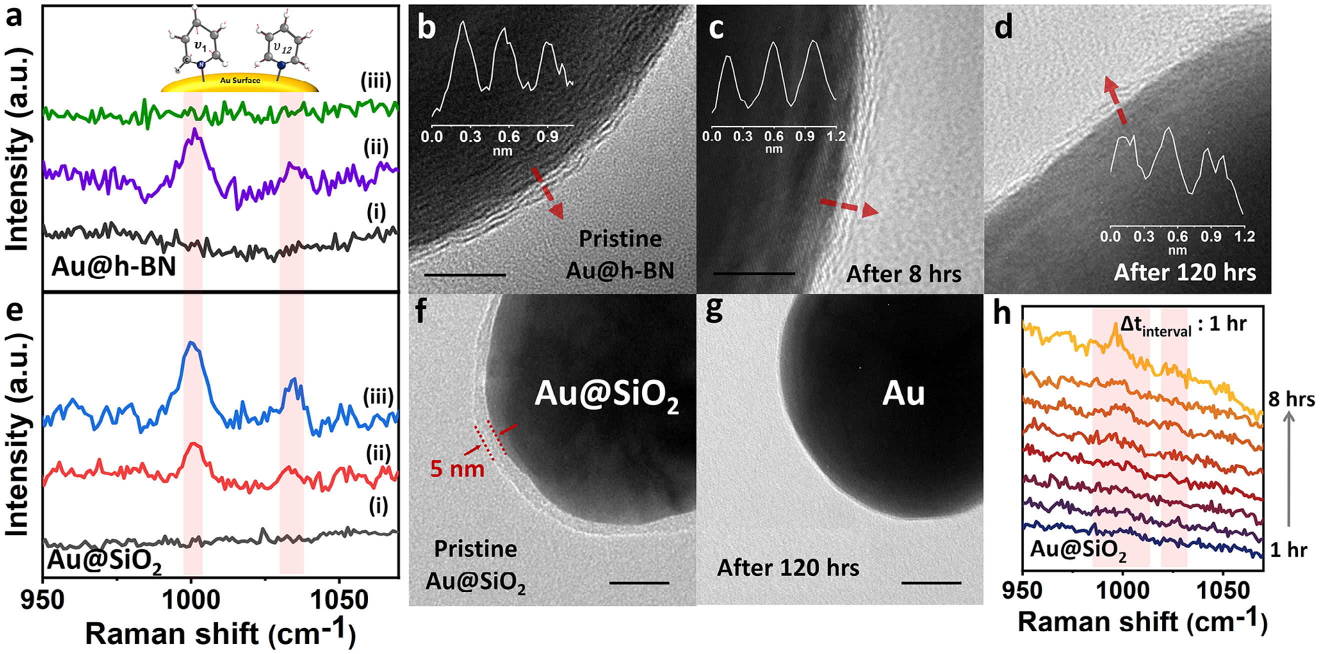

Figure 3. Pinhole detection and alkaline-stability test of Au@h-BN compared with Au@SiO$_2$. a,e) Raman spectra of 25 mM pyridine with Au@h-BN NPs (a) and Au@SiO$_2$ (e) deposited onto Si (i), Au (ii) substrate, and onto Si immersed in a 1.0 M KOH solution for prolonged durations (iii). b–d) HR-TEM images of Au@h-BN before and after dipped in 0.1 M KOH for 8, and 120 h. (Inset) Intensity profiles of h-BN shell region marked by the red-dotted arrow. Scale bar: 5 nm. f,g) TEM images of the Au@SiO$_2$ NPs before and after immersion in a 0.1 M KOH for 120 h. Scale bar: 20 nm. h) Time-dependent Raman spectra of pyridine in the presence of Au@SiO$_2$ NPs deposited onto a Si substrate during immersion in a 1.0 M KOH solution for 8h. The pink-highlighted regions in Figure 3a,e,h indicate peaks associated with the vibrational modes of pyridine.

simulation results indicate that the EF value of Au@h-BN NPs offers ≈4 times higher Raman signal enhancement than that of Au@SiO$_2$ NPs, suggesting their potential for in situ electrochemical Raman applications in any substrates. To further investigate the impact of the dielectric characteristics on Raman signal enhancement, we simulated the EM field distributions of Au@h-BN and Au@SiO$_2$ with varying their shell thickness (Figure 2c). Notably, throughout the investigated thickness range from 1 to 7 nm, Au@h-BN NPs consistently exhibit higher EF compared to Au@SiO$_2$ at the same thicknesses, suggesting that SHINs with a higher dielectric constant exhibit greater Raman scattering enhancement. Although the higher dielectric constant of h-BN compared to that of SiO$_2$ potentially contributes to its enhanced Raman signal effects, the more significant factor in enhancing its performance as a SHINs is likely its extremely low minimum effective thickness (less than 1 nm), which is attributed to its high stability in a 2D geometry and exceptional flexibility compared to conventional dielectric materials.

To verify the integrity of the core–shell structure of Au@h-BN NPs, we conducted tests to confirm the presence of pinholes in the h-BN shell.[32] In the content of SHINs, pyridine is a commonly used chemical molecule for gauging the pinhole-free nature of SHINs.[32] If pyridine is adsorbed onto the surface of the AuNPs, two prominent peaks must appear at ≈1003 and 1034 cm^{-1}.[33] The absence of these peaks would confirm the lack of pinholes in the h-BN shell. No noticeable peaks were observed for the Au@h-BN or Au@SiO$_2$ NPs with thin shell thickness deposited onto the Si substrate (Figure 3a(i),e(i)). In contrast, the results of our tests conducted on pinhole-free Au@h-BN NPs and Au@SiO$_2$ deposited onto an Au substrate revealed the presence of two pyridine peaks (Ring breathing modes, ν_1 and ν_{12}), indicating that pyridine molecules adsorbed onto Au substrate as shown in Figure 3a(ii),e(ii). These results indicate that Au@h-BN with a thickness of 1 nm and Au@SiO$_2$ NPs with a thickness of 2 nm lack any pinholes in their shells. However, Au@SiO$_2$ synthesized in a different batch displayed pyridine-related Raman peaks, suggesting that the reproducible synthesis of pinhole-free Au@SiO$_2$ below a 2 nm-thick shell is challenging.[32] Furthermore, upon immersing the Au@h-BN and Au@SiO$_2$ deposited onto the Si substrate in 0.1 M KOH over 6 h, the Raman spectrum displayed pyridine peaks after several hours for Au@SiO$_2$, not Au@h-BN (Figure 3a(iii),e(iii)). TEM images displayed in Figure 3b–d reveal that the tri-layered h-BN shells remain intact even after immersion in 1.0 M KOH solution for 120 h. In contrast, TEM images of Au@SiO$_2$ after long-term storage in 1.0 M KOH revealed the complete disappearance of the SiO$_2$ shell compared to pristine Au@SiO$_2$ with a thickness of 5 nm (Figure 3f–g). Additionally, time-dependent Raman analysis demonstrated two pyridine peaks emerging after 6 h of KOH treatments (Figure 3h), indicating that the SiO$_2$ shell could be damaged by an alkaline solution.[13b] Consequently, Au@h-BN demonstrates superior stability in alkaline conditions for over 120 h, significantly outperforming conventional Au@SiO$_2$ NPs.

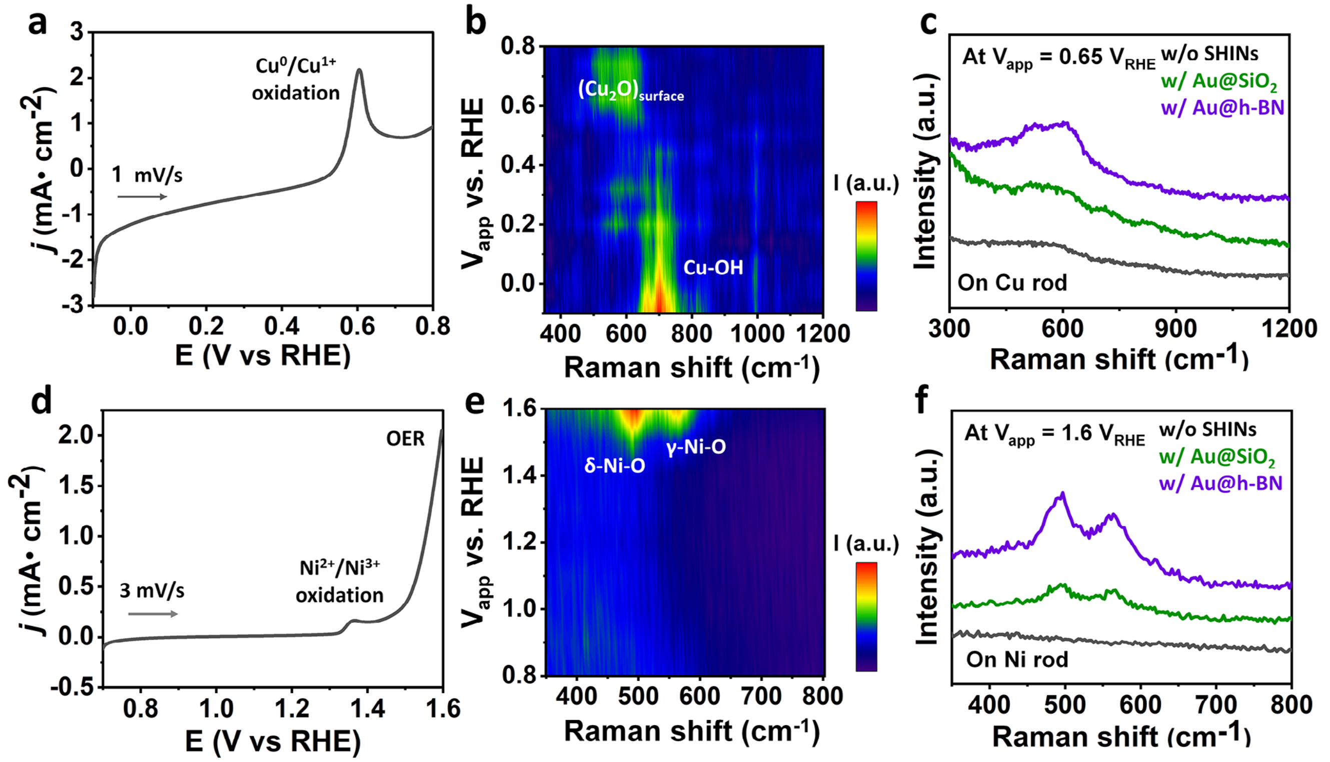

Figure 4. Au@h-BN-assisted in situ Raman analysis of Cu and Ni electrodes in alkaline electrolytes. a) LSV curve of the Cu electrode in the presence of Au@h-BN in 0.1 M KOH. b) Contour map of in situ Raman spectra on Cu recorded during LSV from −0.1 V to 0.8 V versus RHE. c) Comparison of Raman spectra on Cu electrode at the V_{app} of 0.65 V versus RHE without any SHINs (black), with Au@SiO$_2$ NPs (green), and with Au@h-BN NPs (purple). d) LSV curve of the Ni electrode in the presence of Au@h-BN in 0.1 M KOH. e) Contour map of in situ Raman spectra on Ni acquired during LSV (d) from 0.8 to 1.6 V versus RHE. f) Comparison of Raman spectra on Ni electrode at the V_{app} of 1.6 V versus without any SHINs (black), with Au@SiO$_2$ NPs (green), and with Au@h-BN NPs (purple).

2.3. In Situ Electrochemical Raman Spectroscopy Analysis Using Au@h-BN in Alkaline Environments

Electrochemical water splitting in alkaline electrolytes has garnered significant interest because it allows the use of non-noble metal electrodes and offers better corrosion resistance compared to acid-base systems.[34] Therefore, acquiring a fundamental understanding of the mechanisms of electrochemical reactions occurring in alkaline electrolytes is significant. Notably, the long-term stability of Au@h-BN NPs makes them ideal for SHINs utilized in electrocatalysis in extreme environments, particularly alkaline conditions. To explore the potential of Au@h-BN NPs for in situ electrochemical Raman studies under alkaline conditions, we studied the kinetics of oxidation reaction on two metals such as Cu and Ni using Au@h-BN as the standard alkaline electrocatalysis system,[35] particularly focusing on OER for Ni electrode. For this analysis, we employed a custom-built Raman spectrometer, and an in situ Raman cell equipped with a vertically adjustable working electrode holder, along with reference and counter electrodes as shown in Figure S6 (Supporting Information). This setup allowed the working electrode to be positioned close to the glass window, maintaining a 0.2 mm gap to prevent bubble formation through capillary effects.[36] Consequently, this arrangement facilitated effective in situ Raman measurements on the as-known metal electrode during oxidation reaction. The experiments were conducted in a 0.1 KOH electrolyte using a Hg/HgO reference electrode and an Au wire as the counter electrode. Furthermore, in situ electrochemical Raman spectra were obtained on Cu or Ni electrodes as the working electrode by irradiation of a He-Ne laser for 30–60 s during linear sweep voltammetry (LSV) from−0.1 to 0.8 V versus RHE for Cu, and 0.7 to 1.6 V versus RHE for Ni, at an anodic scan rate of 1 mV s^{-1} for Cu, and 3 mV s^{-1} for Ni (**Figure** 4a,d). Here, Au@h-BN and Au@SiO$_2$ NPs were employed as the Raman scattering enhancer materials to compare their activity for enhancement of the Raman signal. In experiments on the Cu electrode, when using Au@h-BN NPs, Raman peak shifts corresponding to Cu─OH and Cu$_2$O were confirmed depending on the applied electrochemical potential (V_{app}) (Figure 4b).[35a] In particular, strong Raman intensity corresponding to Cu─OH appeared at 701 cm^{-1} when the V_{app} is –0.1 V versus RHE; however, their intensity gradually decreased during a positive voltage sweep. At the V_{app} value of 0.6 V versus RHE, Cu$_2$O peaks emerged ranging from 450 to 600 cm^{-1}, indicating the conversion of Cu─OH on the surface of the Cu electrode to Cu$_2$O during the anodic voltage sweep. Notably, the intensity of these peaks was confirmed to be stronger when using Au@h-BN compared to that when without SHINs and using Au@SiO$_2$ (Figure 4c).

In similar experiments on the Ni electrode, when the V_{app} reaches the 1.5 V versus RHE, strong Raman signals appear

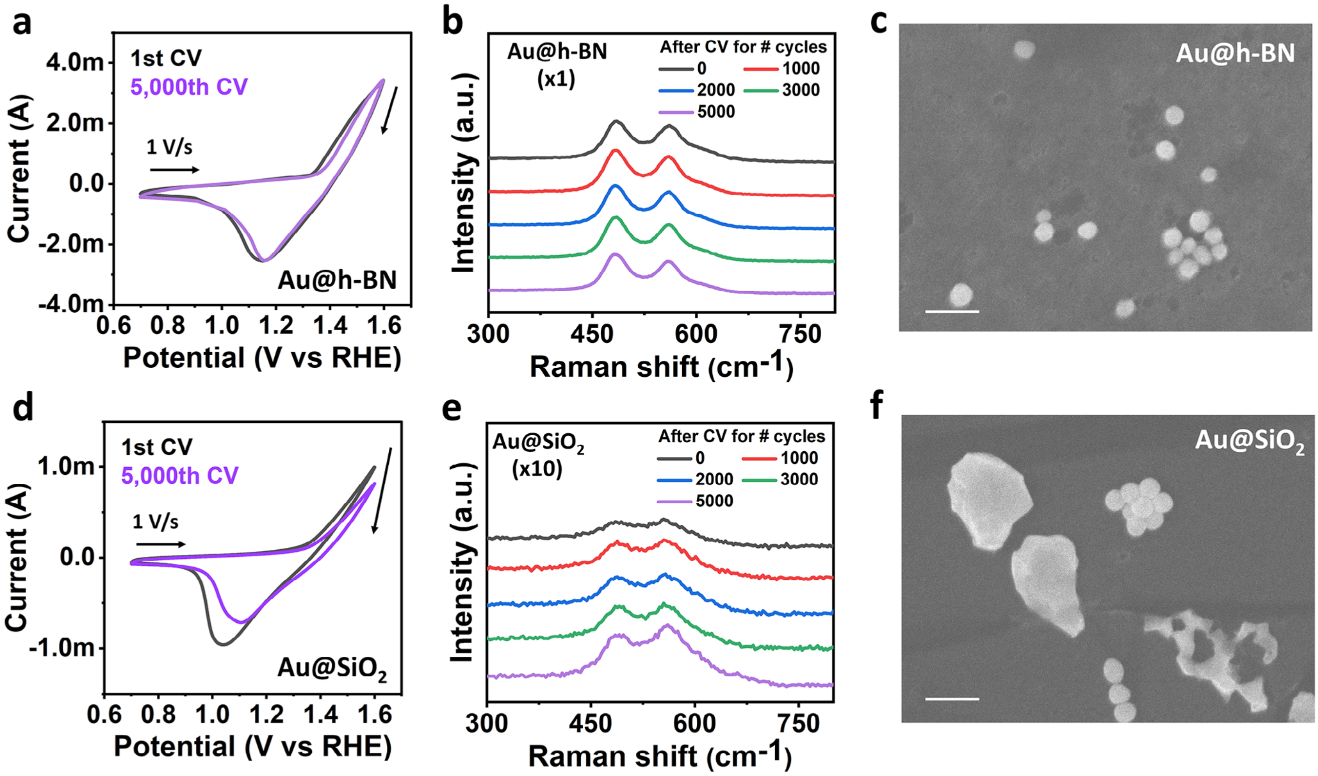

Figure 5. Long-term stability of Au@h-BN and Au@SiO_2 under the alkaline condition. a,d) CV curve of Ni in presence Au@h-BN (a) and Au@SiO_2 (d) at step of st cycle and 5000th cycles. b,e) Raman spectra of Ni electrode with Au@h-BN (b) and Au@SiO_2 magnified 10x (e) at the V_{app} of 1.66 V versus RHE in 1.0 M KOH after *n* cycles of CV (*n* = 0, 1000, 2000, 3000, and 5000). c,f) SEM images of Au@h-BN (c) and Au@SiO_2 (f) after CV 5000 cycles in 1.0 M KOH. Scale bar: 200 nm.

at 494 and 564 cm^{-1} (Figure 4d,e), corresponding to the bending mode (δ) of Ni^{III}-O and the stretching mode (γ) of Ni^{III}-O in NiOOH.[35b,c] These results also highlight the significant role of Ni (III) species in OER catalysis on polycrystalline Ni foils. In addition to these experiments, two control experiments were also performed: in situ Raman measurements without any Raman enhancer materials, and with Au@SiO_2 NPs. As shown in Figure S7 (Supporting Information), no significant peaks were observed without any SHINs even at the V_{app} value of 1.6 V versus RHE. Conversely, when conventional Au@SiO_2 NPs were used, distinct two peaks corresponding to NiOOH were detected above the V_{app} value of 1.5 V versus RHE but with lower intensities compared to those observed with Au@h-BN NPs (Figure 4f). Additionally, we monitored the Raman spectra changes on Ni electrodes subjected to long-term cyclic voltammetry (CV) in the presence of Au@h-BN and Au@SiO_2, respectively (**Figure 5**a,d). These spectra were recorded at the V_{app} of 1.66 V versus RHE after *n* cycles (*n* = 0 to 5000), respectively. When using Au@h-BN, highly enhanced Raman intensities of NiOOH were uniformly apparent even after 5000 cycles (Figure 5b), indicating minimal changes in the Raman spectra over this extensive cycling period. In contrast, when using Au@SiO_2, the Raman signal intensities were relatively weak and increased with the number of cycles (Figure 5e), unlike the spectra of Au@h-BN. In the presence of Au@SiO_2, the Raman peak intensity increased with the progression of CV. The Raman intensity change of Au@SiO_2 can be explained as follows. The SiO_2 shell dissolves in the alkaline solution, resulting in a thinned SiO_2 shell that then causes slightly enhanced EF. However, this enhancement remains lower than that observed with Au@h-BN, likely due to deformation during multiple cycles, as the dissolution of SiO_2 removes the protective layer. Notably, we demonstrated the stability of Au@h-BN and Au@SiO_2 NPs over 5,000th CV cycles as shown in Figure 5. For the Ni electrode within Au@h-BN, there is no significant difference between the 1st and 5,000th cycles (Figure 5a,b), providing evidence that the Au@h-BN NPs do not interfere with the electrochemical stability of the system during in situ experiments. In contrast, a substantial change is observed in CV within Au@SiO_2 (Figure 5d,e), indicating that the presence of Au@SiO_2 NPs influences the electrochemical behavior, and the structural change of Au@SiO_2 causes the reaction environment during prolonged electrochemical reactions. We believe that the negatively charged surface of SiO_2 under alkaline conditions (pH > pK_a of silica surface) substantially affects the electrical double layer formation at the interface between electrode and Au@SiO_2, creating a different electrochemical reaction environment. Rather, the removal of SiO_2 may lead to a recovery of the original CV characteristics. SEM images also reveal the higher stability of Au@h-BN NPs than Au@SiO_2 and bare Au after the multiple cycles (Figure 5c,f; Figure S8, Supporting Information). While the well-dispersed Au@h-BN NPs are observed without observable structural degradation, the morphological changes by agglomeration of SiO_2-dissolved Au NPs are observed after the 5000 cycles. These results indicate that the application of Au@SiO_2 as an adjuvant in fields for long-term in situ electrochemical Raman study could be constrained due to variations in the degree of Raman signal enhancement effects on the thickness of the silica shell during measurements. These findings suggest that Au@h-BN NPs are more suitable for long-term in situ Raman studies, as they do not suffer from chemical instability issues encountered when using Au@SiO_2 NPs. Notably, the Raman peak of NiOOH at the V_{app} persisted even after 10k cycles (Figure S9, Supporting Information), demonstrating the prolonged stability of Au@h-BN NPs under alkaline conditions and their suitability for long-term in situ Raman analysis.

3. Conclusion

In summary, this study comprehensively explores the synthesis, characterization, and enhanced Raman signal properties assisted by Au@h-BN NPs, presenting them as an unprecedented type of SHINs for electrocatalysis analysis in alkaline-base electrochemical reactions. To overcome the limitations of traditional Au@SiO_2 core–shell structures, we successfully utilized h-BN as an efficient protective shell material, leveraging its 2D insulating properties and exceptional chemical stability. Through meticulous control experiments and in-depth spectroscopic and microscopic analyses, we realized the controlled synthesis of Au@h-BN NPs with a targeted shell thickness of ≈1 nm ensuring optimal electrochemical performance. Our findings also emphasize the reproducible pinhole-free characteristics of Au@h-BN NPs, required for SHINERS applications. Particularly, in situ electrochemical Raman spectroscopy analysis revealed the enhanced Raman intensity and long-term stability of Au@h-BN NPs during the oxidation process compared to conventional Au@SiO_2 NPs, underscoring their potential as SHINs for alkaline water electrolysis and other electrochemical processes in extreme conditions. The feasibility of using Au@h-BN in an alkaline environment is anticipated to enhance the current understanding of fundamental electrocatalysis, which accelerates the broader comprehension of electrochemical processes and offers valuable insights into the design and engineering of efficient catalysts for alkaline electrochemical applications.

Supporting Information

Supporting Information is available from the Wiley Online Library or from the author.

Acknowledgements

This work was supported by the National Research Foundation of Korea (NRF) grant funded by the Ministry of Science and ICT, South Korea (NRF-2020M3D1A1110566 21, NRF-2021R1C1C1010603 13, and RS-2023-00220174). Additionally, this research was supported by the Open R&D program of Korea Electric Power Corporation (R23XO04), and the GIST research fund (Future-leading Specialized Research Project, 2025).The analysis of SEM, TEM/EDS, and XPS was performed at the GIST Advanced Institute of Instrumental Analysis (GAIA).

Conflict of Interest

The authors declare no conflict of interest.

Author Contributions

J.H.K. conceived and led the work with guidance from E.L. and H.L. J.H.K. and H.L. led the writing of the paper with assistance by E.L. J.H.K. performed the synthesis of samples and characterization with assistance by J.R., Y.P., and J.Y. XPS analysis was conducted by Y.P., and TEM study was performed by J.Y. and J.H.K. with guidance from E.L. and H.L. FDTD simulations were carried out by J.R. assisted by J.H.K. All authors contributed to the discussions and preparation of the manuscript.

Data Availability Statement

The data that support the findings of this study are available in the supplementary material of this article.

Keywords

alkaline electrolyte, core–shell, hexagonal boron nitride, in situ electrochemical Raman spectroscopy, shell-isolated nanoparticle

Received: February 20, 2025
Published online:

---

[1] H. Adenusi, G. A. Chass, S. Passerini, K. V. Tian, G. Chen, *Adv. Energy Mater.* **2023**, *13*, 2203307.
[2] C. Liu, Z. Neale, G. Cao, *Mater. Today* **2016**, *19*, 109.
[3] S. Wang, A. Lu, C.-J. Zhong, *Nano Converg.* **2021**, *8*, 4.
[4] H. Shen, C. Choi, J. Masa, X. Li, J. Qiu, Y. Jung, Z. Sun, *ChemChem* **2021**, *7*, 1708.
[5] L. R. L. Ting, B. S. Yeo, *Curr. Opin. Electrochem.* **2018**, *8*, 126.
[6] X. Zhang, X. Cheng, Q. Zhang, *J. Energy Chem.* **2016**, *25*, 967.
[7] M. Fleischmann, P. J. Hendra, A. J. McQuillan, *Chem. Phys. Lett.* **1974**, *26*, 163.
[8] J. F. Li, Y. F. Huang, Y. Ding, Z. L. Yang, S. B. Li, X. S. Zhou, F. R. Fan, W. Zhang, Z. Y. Zhou, D. Y. Wu, B. Ren, Z. L. Wang, Z. Q. Tian, *Nature* **2010**, *464*, 392.
[9] a) X.-D. Lin, V. Uzayisenga, J.-F. Li, P.-P. Fang, D.-Y. Wu, B. Ren, Z.-Q. Tian, *J. Raman Spectrosc.* **2012**, *43*, 40; b) M. Gao, Y. Song, Y. Liu, W. Jiang, J. Peng, L. Shi, R. Jia, Y. Muhammad, L. Huang, *Appl. Surf. Sci.* **2021**, *537*, 147912.
[10] a) T. Hartman, B. M. Weckhuysen, *Chem.-Eur. J.* **2018**, *24*, 3733; b) T.-M. Chen, G.-Y. Xu, H. Ren, H. Zhang, Z.-Q. Tian, J.-F. Li, *Nanoscale Adv.* **2019**, *1*, 4522.
[11] a) J. Fernández-Vidal, A. M. Gómez-Marín, L. A. H. Jones, C.-H. Yen, T. D. Veal, V. R. Dhanak, C.-C. Hu, L. J. Hardwick, *J. Phys. Chem. C* **2022**, *126*, 12074; b) B. C. Barlow, B. Guo, A. Situm, A. P. Grosvenor, I. J. Burgess, *J. Electroanal. Chem.* **2019**, *853*, 113559.
[12] T.-J. Li, B.-Y. Wen, Y.-J. Zhang, L. Zhang, J.-F. Li, *J. Raman Spectrosc.* **2022**, *53*, 1386.
[13] a) A. Haryanto, C. W. Lee, *Nano Converg.* **2022**, *11*, 9; b) Y.-H. Wang, S. Li, R.-Y. Zhou, S. Zheng, Y.-J. Zhang, J.-C. Dong, Z.-L. Yang, F. Pan, Z.-Q. Tian, J.-F. Li, *Nat. Protoc.* **2023**, *18*, 883.
[14] a) Y.-J. Zhang, H. Ze, P.-P. Fang, Y.-F. Huang, A. Kudelski, J. Fernández-Vidal, L. J. Hardwick, J. Lipkowski, Z.-Q. Tian, J.-F. Li, *Nat. Rev. Methods Primers* **2023**, *3*, 36; b) Y.-Z. Zhu, R.-Y. Zhou, S. Hu, J.-F. Li, Z.-Q. Tian, *ACS Nano* **2024**, *9*, 32287.
[15] a) Y. Li, K. Burnham, J. Dykes, N. Chopra, *MRS Commun.* **2018**, *8*, 79; b) Y.-J. Zhang, Q.-Q. Chen, X. Chen, A. Wang, Z.-Q. Tian, J.-F. Li, *J. Raman Spectrosc.* **2021**, *52*, 439.
[16] a) L. Li, X. Feng, Y. Nie, S. Chen, F. Shi, K. Xiong, W. Ding, X. Qi, J. Hu, Z. Wei, L.-J. Wan, M. Xia, *ACS Catal.* **2015**, *5*, 4825; b) T. Takashima,

K. Hashimoto, R. Nakamura, *J. Am. Chem. Soc.* **2012**, *134*, 18153; c) T. Subramaniam, B. S. Krishnaveni, S. Devaraj, *J. Mater. Sci.: Mater. Electron.* **2024**, *35*, 1184.

[17] a) P. Wang, Y. Ji, Q. Shao, Y. Li, X. Huang, *Sci. Bull.* **2020**, *65*, 350; b) C. Salvini, M. Re Fiorentin, F. Risplendi, F. Raffone, G. Cicero, *J. Phys. Chem. C* **2022**, *126*, 14441.

[18] Y. Zheng, X. Zhong, Z. Li, Y. Xia, *Part. Part. Syst. Charact.* **2014**, *31*, 266.

[19] a) H. Jeong, D. Y. Kim, J. Kim, S. Moon, N. Han, S. H. Lee, O. F. N. Okello, K. Song, S.-Y. Choi, J. K. Kim, *Sci. Rep.* **2019**, *9*, 5736; b) S. Fukamachi, P. Solís-Fernández, K. Kawahara, D. Tanaka, T. Otake, Y.-C. Lin, K. Suenaga, H. Ago, *Nat. Electron.* **2023**, *6*, 126.

[20] J. F. Moulder, W. F. Stickle, P. E. Sobol, K. D. Bomben, *in Handbook of X-Ray Photoelectron Spectroscopy. Perkin-Elmer Corporation* **1992**.

[21] M. Du, Y. Wu, X. Hao, *Cryst. Eng. Comm.* **2013**, *15*, 1782.

[22] M. Popławski, A. Kwiatkowska, A. Piasecki, *Arch. Metall. Mater.* **2015**, *41*, 60.

[23] P. Buffat, J. P. Borel, *Phys. Rev. A* **1976**, *13*, 2287.

[24] J. S. Lee, S. H. Choi, S. J. Yun, Y. I. Kim, S. Boandoh, J.-H. Park, B. G. Shin, H. Ko, S. H. Lee, Y.-M. Kim, Y. H. Lee, K. K. Kim, S. M. Kim, *Science* **2018**, *362*, 817.

[25] a) M. J. Walsh, K. Yoshida, P. L. Gai, E. D. Boyes, *J. Phys. Conf. Ser.* **2010**, *241*, 012058; b) C. J. Gommes, *Nanoscale* **2019**, *11*, 7386.

[26] a) S. Cao, F. Tao, Y. Tang, Y. Li, J. Yu, *Chem. Soc. Rev.* **2016**, *45*, 4747; b) S. Ali, V. S. Myasnichenko, E. C. Neyts, *Phys. Chem. Chem. Phys.* **2016**, *18*, 792; c) R. Jin, T. Higaki, *Commun. Chem.* **2021**, *4*, 28.

[27] a) E. A. Sutter, P. W. Sutter, *J. Mater. Sci.* **2011**, *46*, 7090; b) S. H. Lee, H. J. Jung, S. J. Lee, J. Theerthagiri, T. H. Kim, M. Y. Choi, *Appl. Surf. Sci.* **2020**, *506*, 145006.

[28] a) M. Shanthil, R. Thomas, R. S. Swathi, K. G. Thomas, *J. Phys. Chem. Lett.* **2012**, *3*, 1459; b) Q. Tran, w.-n. su, K.-J. Chen, C.-J. Pan, J. Rick, C.-C. Chang, B. J. Hwang, *J. Raman Spectrosc.* **2013**, *44*, 1617.

[29] a) O. I. Malyi, M. Boström, V. V. Kulish, P. Thiyam, D. F. Parsons, C. Persson, *Phys. Chem. Chem. Phys.* **2016**, *18*, 7483; b) J. Kischkat, S. Peters, B. Gruska, M. Semtsiv, M. Chashnikova, M. Klinkmüller, O. Fedosenko, S. Machulik, A. Aleksandrova, G. Monastyrskyi, Y. Flores, W. T. Masselink, *Appl. Opt.* **2012**, *51*, 6789.

[30] J. Robertson, *Eur. Phys. J. Appl. Phys.* **2004**, *28*, 265.

[31] A. Laturia, M. L. Van de Put, W. G. Vandenberghe, *npj 2D Mater. Appl.* **2018**, *2*, 6.

[32] J. F. Li, X. D. Tian, S. B. Li, J. R. Anema, Z. L. Yang, Y. Ding, Y. F. Wu, Y. M. Zeng, Q. Z. Chen, B. Ren, Z. L. Wang, Z. Q. Tian, *Nat. Protoc.* **2013**, *8*, 52.

[33] a) J.-F. Li, J. R. Anema, T. Wandlowski, Z.-Q. Tian, *Chem. Soc. Rev.* **2015**, *44*, 8399; b) T. A. Galloway, L. Cabo-Fernandez, I. M. Aldous, F. Braga, L. J. Hardwick, *Faraday Discuss.* **2017**, *205*, 469.

[34] X. Xiao, L. Yang, W. Sun, Y. Chen, H. Yu, K. Li, B. Jia, L. Zhang, T. Ma, *Small* **2022**, *18*, 2105830.

[35] a) N. Bodappa, M. Su, Y. Zhao, J.-B. Le, W.-M. Yang, P. Radjenovic, J.-C. Dong, J. Cheng, Z.-Q. Tian, J.-F. Li, *J. Am. Chem. Soc.* **2019**, *141*, 12192; b) K. Guo, H. Li, J. Huang, Y. Wang, Y. Peng, S. Lu, C. Xu, *J. Energy Chem.* **2021**, *63*, 651; c) J. Xu, B.-X. Wang, D. Lyu, T. Wang, Z. Wang, *Int. J. Hydrogen Energy.* **2023**, *48*, 10724.

[36] Y.-H. Wang, S. Zheng, W.-M. Yang, R.-Y. Zhou, Q.-F. He, P. Radjenovic, J.-C. Dong, S. Li, J. Zheng, Z.-L. Yang, G. Attard, F. Pan, Z.-Q. Tian, J.-F. Li, *Nature* **2021**, *600*, 81.